Hemispheric differences in ozone across the stratosphere-troposphere exchange region

Rodrigo J. Seguel [1, 2], Charlie Opazo [1, 2], Yann Cohen [3], Owen R. Cooper [4], Laura Gallardo [1, 2], Björn-Martin Sinnhuber [5], Florian Obersteiner [5], Andreas Zahn [5], Peter Hoor [6], Susanne Rohs [7], Andreas Marsing [8]

[1]Center for Climate and Resilience Research (CR)[2], Santiago, Chile
[2]Department of Geophysics, Faculty of Physical and Mathematical Sciences, University of Chile, Santiago, Chile
[3]Institut Pierre-Simon Laplace (IPSL), Sorbonne Université/CNRS, Paris, France
[4]NOAA Chemical Sciences Laboratory, Boulder, USA
[5]Karlsruhe Institute of Technology, Institute of Meteorology and Climate Research (IMK), Karlsruhe, Germany
[6]Institute for Atmospheric Physics, Johannes Gutenberg-University, Mainz, Germany
[7]Institute of Energy and Climate Systems 3 – Troposphere (ICE-3), Forschungszentrum Jülich, Jülich, Germany
[8]Institute of Atmospheric Physics, German Aerospace Center (DLR), Oberpfaffenhofen, Germany

Correspondence to: Rodrigo J. Seguel (rodrigoseguel@uchile.cl)

Abstract

Ozone changes in the upper troposphere-lower stratosphere (UTLS) resulting from dynamical and chemical processes strongly affect the atmosphere's radiative forcing. This study analyzed intra- and interhemispheric ozone differences in the UTLS within the 45-60° latitude band, distinguishing between years disrupted by sudden stratospheric warming (SSW) events from 2002 to 2022. We utilized measurements from IAGOS commercial aircraft (45-60 ºN), long-term ozonesonde records (45-60 ºS) and unique in situ measurements from the High Altitude and Long Range (HALO) research aircraft deployed over the southernmost region of South America (45-60 ºS) in September-November 2019 as a part of the Southern Hemisphere Transport, Dynamics, and Chemistry (SouthTRAC) research campaign. The mission period enabled us to examine the impact of two Southern Hemisphere (SH) SSW events developed during 2002 and 2019. To enhance the spatial coverage, we incorporated CAMS reanalysis data. Stratospheric air character was assigned using relative humidity (<20%) and carbon monoxide (<50 nmol mol^{-1}) thresholds. Our results show that air masses of stratospheric origin had higher ozone abundances in the Northern Hemisphere (NH) UTLS than in the SH (between 300-200 hPa and 45-60° latitude): In high ozone depletion years in the stratospheric vortex, the SH ozone median (184 nmol mol^{-1}) was only 54% of that in the NH (341 nmol mol^{-1}), while in low depletion years, SH ozone median (214 nmol mol^{-1}) reached 57% of the NH values (371 nmol mol^{-1}). Notably, the SSW events (2002 and 2008) increased SH UTLS ozone by 24% (43 nmol mol^{-1}) compared to high depletion years, while in the NH, the increase was 9% (31 nmol mol^{-1}).

1 Introduction

Ozone (O_3) has generated an effective radiative forcing (ERF) of +0.47 [0.24 to 0.71] W m^{-2} over the industrial era, from 1750 to 2019. The ERF for ozone represents 17% of the total anthropogenic ERF change, estimated at +2.72 [1.96 to 3.48] W m^{-2} (Forster et al., 2021). The ozone abundance in the troposphere is related to the atmosphere's oxidizing capacity and is closely associated with methane abundance, the second strongest greenhouse gas, due to hydroxyl radical (·OH) reactions (Saunois et al., 2020). At ground level, short-term exposure to ozone impairs human lung function and contributes to developing asthma symptoms in susceptible people (McConnell et al., 2002; Zheng et al., 2021). Total global mortality due to long-term ozone exposure has been estimated at 365,000 [175,000 to 564,000] deaths in 2019 (Health Effects Institute, 2020).

The tropospheric ozone budget is controlled by chemical production and loss, dry deposition and stratosphere-troposphere exchange (STE) (Archibald et al., 2020). Oxidation of volatile organic compounds (VOC) initiated by hydroxyl radicals lead to tropospheric ozone formation. During this process, hydroperoxyl (HO_2) and alkyl peroxy radicals (RO_2) reactions with nitric oxide (NO) yield nitrogen dioxide (NO_2), which photolyzes to produce ozone (Monks et al., 2015). In the troposphere, the chemical loss results mainly from ozone photolysis ($\lambda \leq 320$ nm) and ozone reaction with hydroxyl and hydroperoxyl radicals (Atkinson, 2000). An important ozone sink is dry deposition at the surface (Clifton et al., 2020).

The STE, estimated at 284 ±193 Tg O_3 year^{-1} (Griffiths et al., 2021; Szopa et al., 2021), is comparable with the net chemical ozone production in the troposphere. STE involves several mechanisms, including tropopause folds within mid-latitude cyclones, cutoff-low decay and gravity wave breaking (Archibald et al., 2020; Cooper et al., 2004; Stohl et al., 2003). STE shows strong geographical asymmetry and seasonal cycles. STE dominates in the extratropics, with hotspots in mountain regions of North and South America, over the Tibetan Plateau and in the storm tracks over the North Atlantic Ocean and North Pacific Ocean, which are more intense in winter and early spring in both hemispheres (Škerlak et al., 2014).

The poleward expansion of the SH Hadley circulation has also been proposed as a mechanism able to enhance downward transport of ozone from the stratosphere to the troposphere at higher latitudes (Lu et al., 2019). STE's contribution to the tropospheric ozone budget is expected to increase due to declining levels of ozone-depleting substances (ODS) and the Brewer-Dobson circulation (BDC) acceleration, especially in the lower stratosphere, caused by increasing greenhouse gas emissions (Butchart, 2014). In contrast, simulations based on climate models do not show BDC acceleration in the mid-stratosphere of the mid-latitude NH since the late 1980s due to declining ODS and the timing of volcanic eruptions (Garfinkel et al., 2017).

Ozone changes in the upper troposphere-lower stratosphere (UTLS) strongly impact the radiative forcing of the atmosphere (Riese et al., 2012; Skeie et al., 2020). Therefore, in situ measurements in the UTLS, characterized by bidirectional trace gas exchange (Gettelman et al., 2011), are crucial to reducing the uncertainty of chemistry climate models and validating satellite retrievals (Bourgeois et al., 2020). Unfortunately, in the Southern Hemisphere, measurements from IAGOS (In-service Aircraft for a Global Observing System: Petzold et al., 2015) commercial aircraft rarely extend beyond 35ºS, and only a few aircraft-based research missions have characterized UTLS chemical composition in this area. The HALO (High Altitude and LOng

range) aircraft measured dry air masses descending from the stratosphere down to an altitude of 7 km a.s.l. over the Antarctic in September 2012 (Rolf et al., 2015). Also, flights over the South Atlantic and South Pacific Oceans conducted by the Atmospheric Tomography (ATom) mission measured a higher frequency of stratospheric intrusions during spring (Bourgeois
70   et al., 2020). In addition, valuable long-term vertical ozone profiles have been obtained through ozonesonde launches at remote sites in higher latitudes of the SH, such as the Ushuaia (Argentina), Lauder (New Zealand) and Macquarie Island (Australia) stations, since 2008, 1986 and 1994 respectively (Zeng et al., 2024; Van Malderen et al., 2024).

In this context, the research project Southern Hemisphere Transport, Dynamics, and Chemistry (SouthTRAC) was designed to comprehensively study the dynamical and chemical processes in the SH UTLS region using the HALO instrumented aircraft
75   during the late winter and spring seasons (September-November) of 2019 (Rapp et al., 2021). SouthTRAC coincided with a polar stratospheric sudden warming (SSW) event that occurred in September 2019 (Rao et al., 2020; Rapp et al., 2021). SSW in the SH is a phenomenon that is unusual compared with the higher frequency of SSW events in the NH, with approximately one event per decade in the SH versus six in the NH (Dunn et al., 2020; Charlton and Polvani, 2007). SSW is caused by wave events that can decelerate the westerly polar night jet and warm the polar stratosphere by descending motion, resulting in
80   reduced heterogeneous active chlorine formation onto polar stratospheric clouds and less catalytic ozone depletion (Scambos and Stammerjohn, 2020). Accordingly, the annual mean total ozone reported in 2019 was 65 DU higher than the long-term average, at 60º-90ºS (Dunn et al., 2020). The mission also coincided with intense Australian bushfires and biomass-burning events in central South America, which produced plumes detected by HALO in the UTLS (Kloss et al., 2021; Johansson et al., 2022).

85   Ozone in the UTLS is highly variable, driven by a complex interplay of dynamical and chemical processes (Millán et al., 2024; Bourgeois et al., 2020; (Neu et al., 2014); Riese et al., 2012). In this context, SSW events represent a diminished ozone depletion scenario, which, combined with the highly resolved profiles obtained during the SouthTRAC campaign, provides a unique and realistic framework for assessing ozone changes. In this study, we leverage the increased ozone abundance under low-depletion conditions derived from SSW events to determine the effect on the ozone mixing ratio in UTLS of both
90   hemispheres. This comparative analysis is based on stratospheric and tropospheric chemical traces measured during the SouthTRAC mission, by IAGOS commercial aircraft and by from ozonesondes, focusing on the 45-60° latitude band. Spatial coverage is further enhanced using the Copernicus Atmosphere Monitoring Service reanalysis (CAMSRA), which is compared against in situ measurement. Specifically, we quantified the ozone mixing ratios in air masses exhibiting stratospheric character and examined the interannual variability between years of high and low ozone depletion disrupted by SSW events.
95   Furthermore, by characterizing ozone and chemical species exchange in the UTLS, we identified a valuable dataset for evaluating the models that simulate ozone transport from the stratosphere to the troposphere in both hemispheres.

2 Data

2.1 SouthTRAC data

The SouthTRAC mission was conducted mainly over the southernmost region of South America within the latitudinal and
100 meridional band 45º-60ºS and 30º-85W, respectively (**Fig. 1**). During this mission, the HALO aircraft was equipped with 13
instruments for sampling the physical and chemical properties of the atmosphere. This research focuses on the measurements
of ozone, carbon monoxide (CO), water vapor, nitric acid (HNO$_3$) and hydrogen chloride (HCl). The number of measurements
of each species is presented in Table 1.
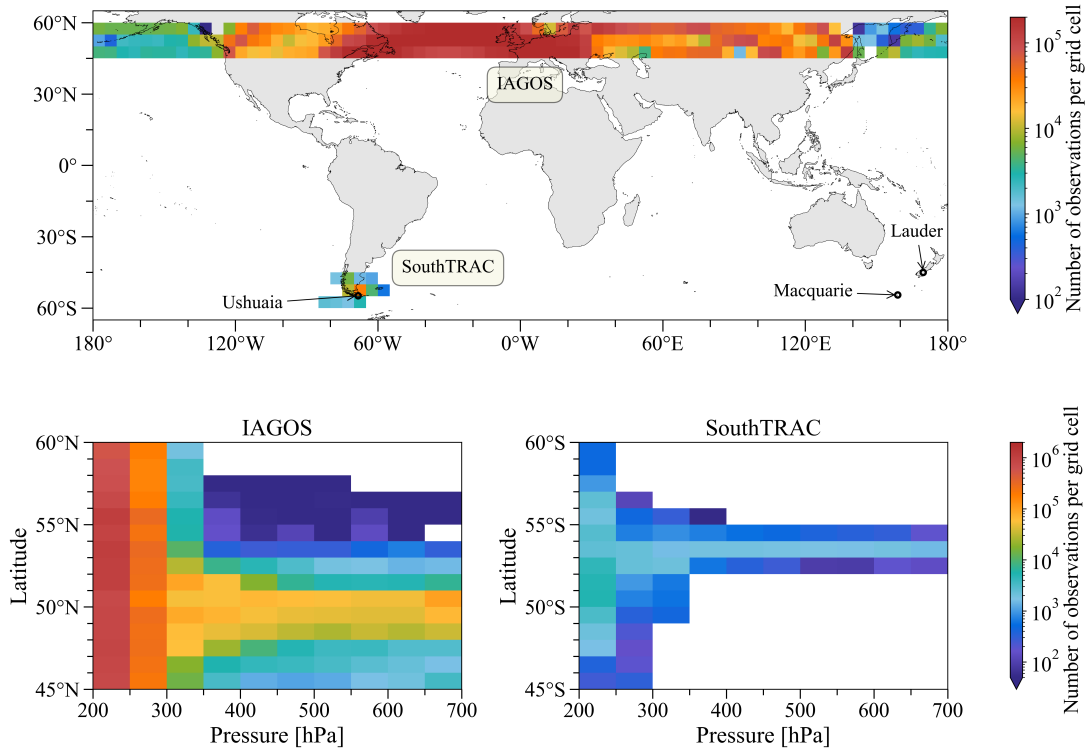
105 **Figure 1: Routes position frequency obtained from aircraft GPSs. All panels show only SouthTRAC and IAGOS data within the
same latitudinal band 45º-60º in the SH and NH. The upper panel shows the number of GPS observations by grid cell (5º x 5º)
between 700 and 200 hPa. The lower panels show the number of GPS observations in every grid cell (1º x 50 hPa) between 700 and
200 hPa for IAGOS (left) and SouthTRAC (right). The upper panel also indicates the location of the ozonesonde sites of Ushuaia,
Lauder and Macquarie Island.**

110 In situ ozone was measured by the Fast AIRborne Ozone monitor (FAIRO) provided by the Karlsruhe Institute of Technology
(KIT). FAIRO combines two measurement principles: UV ozone absorption at 255 nm and dry chemiluminescence from the
reaction of ozone with an organic dye (coumarin) at 500 nm (Ermel et al., 2013). In this dual configuration, the UV photometer
calibrated the chemiluminescence response. We utilized ozone records measured by chemiluminescence due to their higher
sampling frequency (5 Hz) compared with UV photometry (0.25 Hz). Typical one standard deviation (1σ) measurement

precision is 0.08 nmol mol^{-1} for the UV spectrometer measuring at 0.25 Hz and ~0.05 nmol mol^{-1} for the chemiluminescence detector measuring at 5 Hz, 1 bar and 5 nmol mol^{-1} absolute mixing ratio (Zahn et al., 2012). The estimated uncertainty for UV photometer measurements was 2% and for the combined techniques (UV and chemiluminescence) was 2.5%.

The University of Mainz Airborne Quantum Cascade Laser Spectrometer (UMAQS) measured in situ carbon monoxide. This instrument is based on direct absorption in the near-infrared through a continuous-wave quantum cascade laser (Müller et al., 2015). The instrument had a typical carbon monoxide precision of 0.68 nmol mol^{-1} (2σ), an accuracy of 1.2 nmol mol^{-1} and a total uncertainty of 1.4 nmol mol^{-1}.

Static pressure and static temperature were measured by Basic HALO Measurement and Sensor System (BAHAMAS) with an estimated accuracy of 0.3 hPa and 0.5 K, respectively (Giez et al., 2017; Kaufmann et al., 2018). BAHAMAS also measured water vapor at the absorption line of 1.37 μm using the Sophisticated Hygrometer for Atmospheric ResearCh (SHARC), a tunable diode laser hygrometer. The limit of detection of SHARC measurement achieved during SouthTRAC campaign was 2 μmol mol^{-1} with an absolute uncertainty of ±1 μmol mol^{-1} (Kaufmann et al., 2018).

Nitric acid and hydrogen chloride were measured using the Airborne Chemical Ionization Mass Spectrometer (AIMS). In this system, the ion source generates reagent ions (SF_5^-) that selectively react with HNO_3 and HCl to form $HFNO_3^-$ and $HFCl^-$, respectively. A fast quadrupole mass spectrometer then separates the ion products based on their mass-to-charge ratio. Typical accuracy, precision (1σ), and limit of detection are 16%, 20%, and 20 pmol mol^{-1} for HNO_3 and 12%, 16%, and 15 pmol mol^{-1} for HCl, respectively (Jurkat et al., 2016).

2.2 Ozonesonde data

Ozone profiles from ozonesondes launched at Ushuaia, Argentina (54.85 ºS, 68.31 ºW) and Macquarie Island, Australia (54.50 °S, 158.95°E) were obtained from the World Ozone and Ultraviolet Radiation Data Centre, WOUDC (https://woudc.org/) while ozone profiles from Lauder, New Zealand (45.04 °S, 169.68 °E) were obtained from the so-called initiative Harmonization and Evaluation of Ground Based Instruments for Free Tropospheric Ozone Measurements (HEGIFTOM). These data were included in our research in order to compare SouthTRAC measurements to historical data.

These ozonesondes were coupled with radiosondes, which measured pressure, temperature, RH, wind speed and wind direction. **Table 1** shows the available periods utilized in this study and the number of validated flights from each site. The ozonesondes were linearly interpolated to an altitude grid with intervals of 50 m (Ohyama et al., 2018).

During 2002-2022, several radiosonde models were utilized interchangeably (e.g., Lauder). The Vaisala RS92 and its replacement RS41 sensor are among the most frequently used models. Regarding RH, the latter performs better than the older version, particularly in cloudy conditions (Jensen et al., 2016). Overall, both sensors have an uncertainty of 5% and show a consistent difference of about 1-2%, with the RH of the RS41 almost always greater than RS92 (Jensen et al., 2016).

145 **Table 1**: Summary of data used. The columns detail dataset sources, spatial coverage, temporal periods, the number of flights in the period and the number of measurements for each variable (in ozonesondes is the number of interpolated measurements) between 200-300 hPa.

Data source	Hemisphere or site (lat., lon.)	Periods	No. flights or valid launches	Variable (No. measurements)
SouthTRAC	SH (45ºS-60ºS, 30ºW-85ºW)	4 Sep - 20 Nov 2019	16	Pressure: 43k O$_3$: 39k CO: 26k H$_2$O: 43k RH: 43k
WOUDC	1. Ushuaia (54.85ºS, 68.31ºW), 2. Lauder (45.04ºS, 169.68ºE), 3. Macquarie (54.50ºS, 158.95ºE)	1. 2008-2022 2. 2002-2022 3. 2002-2022	1. 141 2. 232 3. 203	1. Pressure: 7.1k O$_3$: 7.1k RH: 7.1k 2. Pressure: 12k O$_3$: 12k RH: 12k 3. Pressure: 11K O$_3$: 11k RH: 11k
IAGOS	NH (45°N-60°N)	2002-2022	6,315	Pressure: 16M O$_3$: 11M CO: 11M H$_2$O: 14M RH: 15M

2.3 IAGOS data

The IAGOS research infrastructure provides in situ measurements of chemical species on board several commercial aircraft. IAGOS is a continuation of the former observation systems MOZAIC (Measurement of Ozone and Water Vapor by Airbus

150 In-Service Aircraft: Marenco et al., 1998) and also includes the CARIBIC measurement system (Civil Aircraft for the Regular Investigation of the Atmosphere Based on an Instrument Container: Brenninkmeijer et al., 1999, 2007; Stratmann et al., 2016), now called IAGOS-CORE and IAGOS-CARIBIC.

The MOZAIC observations started in August 1994 for ozone and water vapor on board five equipped aircraft, whereas the carbon monoxide measurements started in December 2001. The CARIBIC observations started in 1997 for a wide range of

155 chemical species, including ozone, water vapor and carbon monoxide, on a single aircraft.

IAGOS-CORE provides ozone (and carbon monoxide) data using an ultraviolet (infrared) absorption spectrometer, with an accuracy, precision and time response of 2 nmol mol^{-1}, 2% and 4 s (5 nmol mol^{-1}, 5%, 30 s) respectively (Nédélec et al., 2003; Nédélec et al., 2015; Thouret et al., 1998). Water vapor is measured with a capacitive hygrometer, characterized by an accuracy of 5% in RH with respect to liquid water (RHL), or 6% RHL in the vicinity of the thermal tropopause at midlatitudes, and a

160 time response of 5 – 300 s (Helten et al., 1998; Neis et al., 2015; Rolf et al., 2024; Smit et al., 2014).

IAGOS-CARIBIC uses the identical instrument to measure ozone as described for HALO (see section 2.2). Carbon monoxide data are measured by a commercial resonance fluorescence UV instrument modified for use onboard commercial aircraft. Its

accuracy, precision and time response are respectively less than 2 nmol mol^{-1}, 1 – 2 nmol mol^{-1}, and less than 2 s (Scharffe et al., 2012). Water vapor measurements are performed with a photoacoustic laser spectrometer and a frost-point hygrometer, with an accuracy of less than 4 % or 0.3 μmol mol^{-1} for the mixing ratio. The time response varies between 5 and 30 s for humid (>100 ppm) and dry air masses (<10 ppm) respectively (Dyroff et al., 2015; Zahn et al., 2014).

2.4 CAMS & ERA5 reanalysis

We utilized vertical ozone profiles, temperature and specific humidity from the chemical reanalysis CAMSRA (Copernicus Atmosphere Monitoring Service, reanalysis). CAMSRA has 60 model levels from the surface to the top of the atmosphere, a horizontal resolution of 0.75° x 0.75° and a time resolution every 3 hours (Inness et al., 2019). We also retrieved zonal wind at 60°N (60°S) and 10 hPa from ERA5 reanalysis (Hersbach et al., 2023). ERA5 has hourly resolution, 0.25° x 0.25° horizontal resolution and 37 pressure levels. We used post-processed daily mean on pressure levels obtained from Copernicus Climate Change Service (C3S) Climate Data Store (CDS).

3 Method

3.1 Study period & UTLS definition

The mission had two stages: 9 Sep-6 Oct 2019 and 6-15 Nov 2019, totaling 16 flights, coinciding with the maximum ozone depletion in Antarctica. The UTLS portion studied ranged between 200 (~12 km) and 300 (~9 km) hPa. For comparison, IAGOS data from 2002 to 2022 were analyzed for the same latitudinal band and altitude range in the NH. **Figure 1** shows the sampling density given by the aircraft's positional data to identify those regions of the atmosphere with more data availability. In addition, **Figure S1** in the Supplement depicts the highest number of GPS observations obtained between 300 and 200 hPa compared to the range of 700 to 300 hPa.

3.2 High and low ozone depletion years definition

We distinguished low ozone depletion years from high ozone depletion years according to the occurrence of SSW events. Therefore, we applied the definition proposed by (Charlton and Polvani, 2007) and used ERA5 data to detect major SSW, which is based on determining the reversal of the daily-mean, zonal-mean zonal winds from westerly to easterly at 60ºN and 10 hPa from November to April. **Table 2** shows the so-called central date (Charlton and Polvani, 2007), i.e., the first day on which the daily zonal mean zonal wind at 10 hPa and 60°N changed from westerly to easterly between November and March. During the detection procedure, we required 20 consecutive days with westerly winds before identifying another event. We excluded cases with easterly zonal winds that did not return to westerly for at least 10 consecutive days before 30 April. In the SH, the shift from westerly to easterly is considered between July and October, and we excluded the cases when the wind did not return to westerly by 30 November.

In addition to the 2002 major SSW identified by the above metric, this research also considered the 2019 SH SSW as a low ozone depletion year. While the 2019 event did not reverse the zonal wind at 60ºN and 10 hPa, the weakening of the stratospheric polar vortex was as strong as that of the 2002 event (Lim et al., 2021; Rao et al., 2020).

195 Additionally, given that the ozone-depleted air masses typically reach their minimum ozone content in October (March) of the Southern (Northern) hemisphere, we split the flights into late winter-early spring and mid-spring, representing the latter, the period when depleted ozone air likely reaches the SouthTRAC study region (**Table 2**).

Table 2: Study period considered for both hemispheres, subperiods and low ozone depletion years according to SSW definition.

Study period	Late winter-early spring (no. flights or launches)	Mid spring (no. flights or launches)	Low-depletion years (central date)
4 Mar - 20 May	4 - 31 Mar (456 flights)	1 Apr – 20 May (835 flights)	2002 (17 Feb), 2003 (18 Jan), 2004 (5 Jan), 2006 (21 Jan), 2007 (24 Feb), 2008 (22 Feb), 2009 (24 Jan), 2010 (24 Mar), 2013 (6 Jan), 2018 (12 Feb), 2019 (1 Jan) and 2021 (5 Jan)
4 Sep - 20 Nov	4 - 30 Sep (10 flights) (204 launches)	1 Oct - 20 Nov (6 flights) (372 launches)	2002 (25 Sep) and 2019[†] (15 Sep)

[†]: Central date determined when the zonal-mean zonal winds at 60°S and 10 hPa decrease to $\leq$ 20 m/s (Rao et al., 2020).

200 **3.3 Stratospheric character determination**

We utilized several sensors with different accuracies to filter air masses by RH. Vaisala radiosonde sensors have a longer response time, and their vertical resolution highly depends on temperature; thus, radiosonde sensors are less accurate than SHARC, IAGOS-CORE, and IAGOS-CARIBIC measurements. Therefore, we tested different relative humidity levels, from 50% to 10% (every 10 intervals), to effectively filter tropospheric moist mid-latitude air masses. We estimated that a RH lower

205 than 20% is effective in excluding tropospheric air masses richer in water vapor and is sufficiently conservative, given the sensor accuracy. This threshold behaves similarly to the 50 nmol mol^{-1} carbon monoxide filter (analyzed in more detail in Section 3.2).

CAMSRA profiles were also filtered using 20% RH for the 45°N-60°N and 45°S-60°S zonal bands between 2003 and 2022 (Table 1). In this case, we calculated the relative humidity with respect to liquid water from temperature and specific humidity.

210 **4 Results and discussion**

In the following sections, we mainly used the relative humidity to assign the stratospheric air character in the UTLS. At the same time, in some specific events, we also take advantage of the enhanced trace gases simultaneously measured, at high time resolution, on board HALO to further characterize the tropospheric or stratospheric origin of the air masses.

4.1 Ozone, carbon monoxide and water vapor overview

Tracer-to-tracer scatterplots between stratospheric ozone tracer and tropospheric tracers, such as water vapor and carbon monoxide at two pressure intervals, are shown in **Figures 2** and **3**. Stratospheric and tropospheric tracer scatterplots have been used in previous works to provide a magnitude of bidirectional exchange across the tropopause by the identification of stratospheric and tropospheric branches and mixed air regions according to the tracer abundances (Gettelman et al., 2011).

In general, we observed higher ozone values in the UTLS and free troposphere of the NH compared to the SH. Scatterplots show that ozone between 300-200 hPa in the SH rarely exceeds 400 nmol mol^{-1}. In contrast, in the NH, high ozone levels near 1200 nmol mol^{-1} associated with low water vapor levels (i.e., drier air) are observed. The same pattern is observed between 700 and 300 hPa, with ozone levels in the NH much higher than observed in the SH (up to an excess of 200 nmol mol^{-1}). **Figure 2** also shows a similar relationship between ozone and water vapor in low and high-depletion years at both pressure intervals in the NH. In the following section, we clearly distinguish the ozone differences between the low and high-depletion years.
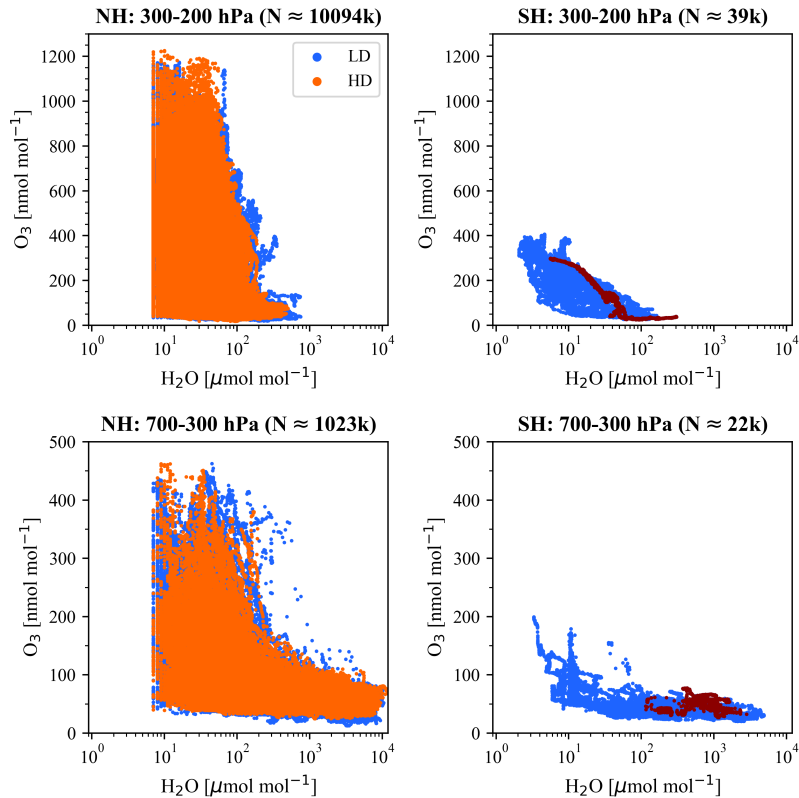
Figure 2: Scatter plots of ozone versus water vapor. The left panels show scatter plots for the NH between 300-200 and 700-300 hPa (IAGOS data set described in Table 1). The right panels show the same for the SH (SouthTRAC data described in Table 1). Low and high-depletion (LD and HD) years are in blue and orange colors, respectively. Above each plot, N stands for the number of observations. In the SH, the flight conducted on 12 Nov 2019 is highlighted in dark red.

Tracer-to-tracer scatterplots of ozone and carbon monoxide show that in the NH, carbon monoxide reaches higher levels (~300 nmol mol^{-1}) at both 300-200 and 700-300 hPa (**Figure 3**). Notice that some carbon monoxide values are not included in NH because they were not simultaneously measured with ozone. Again, carbon monoxide and ozone show a similar relationship in low and high-depletion years in the NH. In contrast, in the SH, carbon monoxide rarely exceeds 100 nmol mol^{-1} in both pressure intervals (300-200 hPa and 700-300 hPa). An exception to this behavior was observed during the flight conducted on 12 Nov 2019 (mid-spring), which detected elevated levels of carbon monoxide (>200 nmol mol^{-1}), ozone (>100 nmol mol^{-1}) and water vapor (>100 μmol mol^{-1}) above 9 km. These elevated levels were attributed to tropospheric plumes and may have been pyrogenic in origin, given the simultaneous bushfires in Australia that extended from Sep 2019 to Mar 2020 (Kloss et al., 2021). Ultimately, the impact of emissions from the Australian bushfires in the UTLS may be interpreted as feedback initiated early in August-September 2019, which derived from the deceleration of the polar vortex in the middle stratosphere.
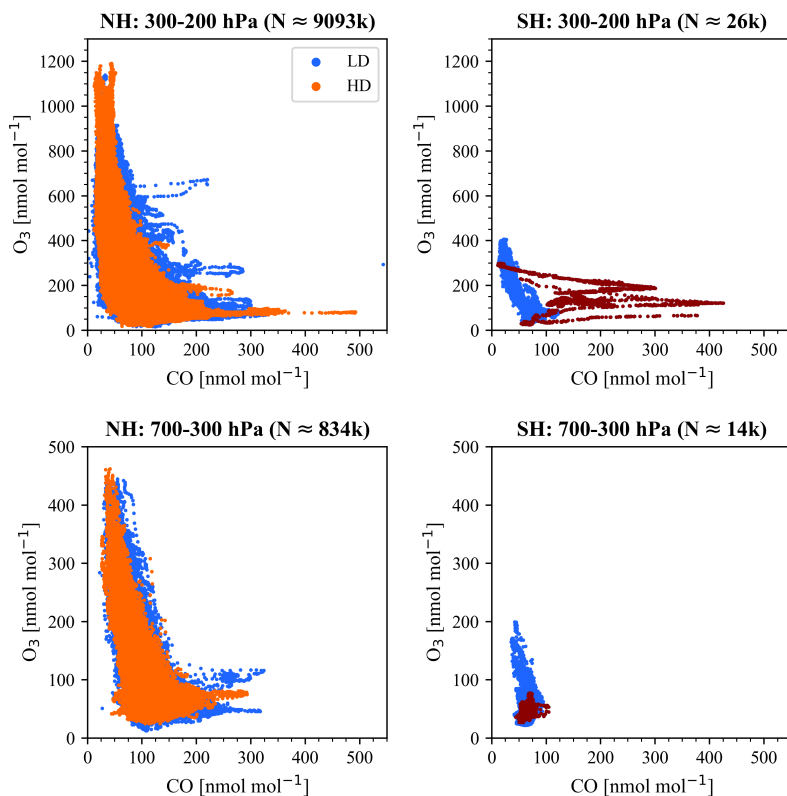
Figure 3: Scatter plots of ozone versus carbon monoxide. The left panels show scatter plots for the NH between 300-200 and 700-300 hPa (IAGOS data set described in Table 1). The right panels show the same for the SH (SouthTRAC campaign data described in Table 1). Low and high-depletion (LD and HD) years are in blue and orange colors, respectively. Above each plot, N stands for the number of observations. In the SH, the flight conducted on 12 Nov 2019 is highlighted in dark red.

In this regard, the abundance of nitric acid and hydrogen chloride are also useful in determining the plume's origin since these two species are stable in the stratosphere but more prone to removal in the troposphere. Tracer-to-tracer scatterplots of these

species versus ozone and carbon monoxide (**Fig. 4**) show that nitric acid and hydrogen chloride were generally higher when ozone was higher and lower when carbon monoxide was higher. This anticorrelation between carbon monoxide and stratospheric tracers suggests that this plume predominantly originates from the troposphere. Nevertheless, we cannot entirely exclude the mixing processes of stratospheric and tropospheric air masses, as shown by the fluctuations registered during the flight (**Fig. 4**).

Hence, the NH has higher carbon monoxide levels than the SH and a threshold of 50 nmol mol^{-1} at 300-200 hPa seems to well represent the stratospheric branch in both Hemispheres (**Fig. 3**). Accordingly, we utilized the carbon monoxide levels (<50 nmol mol^{-1}) in the following section to distinguish stratospheric air masses, even though our primary classification relies on the RH threshold.
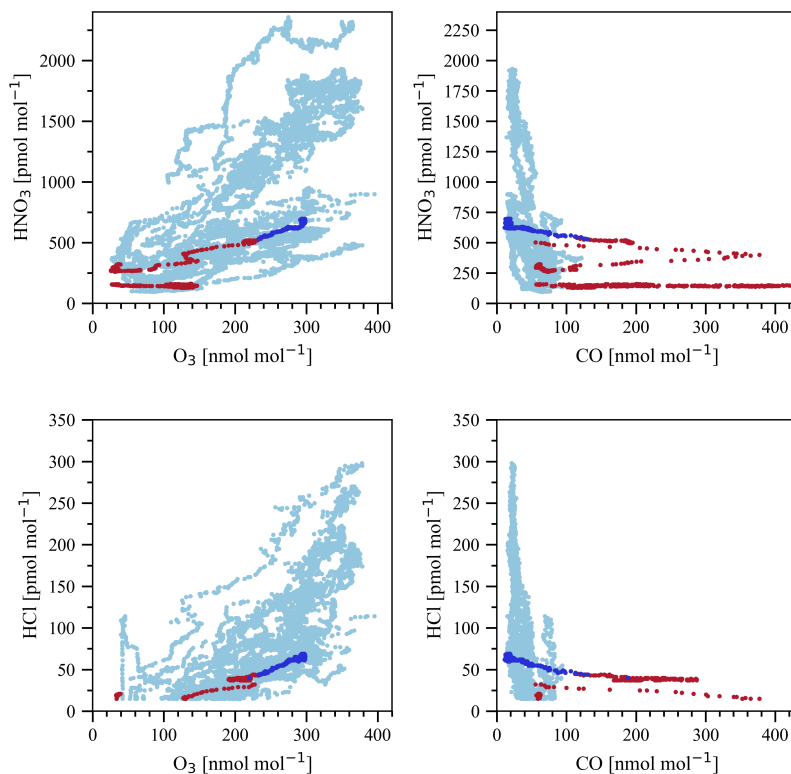
Figure 4: Scatter plots of nitric acid versus ozone, nitric acid versus carbon monoxide, hydrogen chloride versus ozone and hydrogen chloride versus carbon monoxide. Measurements obtained during the flight conducted on 12 Nov 2019 (ST25) are highlighted from the other flight measurements depending on their relative humidity in blue (< 20%) or in red (> 20%).

4.2 Stratospheric ozone in the UTLS

As discussed earlier in the methodology, aircraft RH observations are more accurate than radiosondes. Therefore, we tested several RH filters on the air masses, aiming to minimize the impact of the reported error of the sensors within the UTLS and

to minimize the inclusion of tropospheric air. The following discussion is based on a 20% RH filter, while results for 30% and 10% RH are shown in the Supplement **(Fig. S2 and S3)**. **Figure 5** depicts ozone boxplots and the corresponding observation numbers (in the 10-base logarithm) by pressure bins. It is worth noting that the pressure bins between 300 y 280 hPa have less data, particularly those obtained from aircraft sampling **(Fig. 5)**, which implies a lower representativity at the lowest altitude bins. The same observation applies to the 230-220 hPa bin during mid-spring in the SouthTRAC mission. In the appendix (**Fig. A1**), we also present the ozone boxplots without filters to visualize the aspect of the original data.
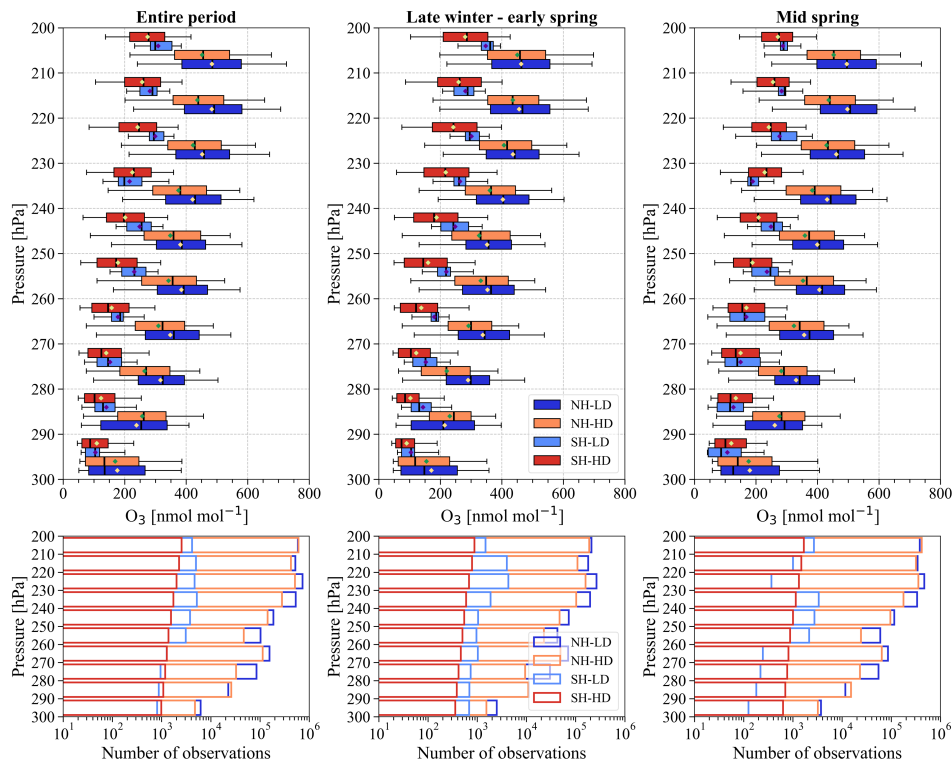
Figure 5: Ozone box plot (nmol mol^{-1}) and associated sample sizes by pressure bins. The plots include ozone data with RH less than 20% obtained from IAGOS, SouthTRAC and WOUDC (Table 1). In the upper panel, the left, middle and right plots show the entire period, late winter-early spring and mid-spring respectively, for the northern and southern hemispheres and high-depleted (HD) and low-depleted (LD) years. Box plots indicate the median, the 25th and 75th percentiles. The diamonds in the upper panels indicate the mean values. The whiskers extend to the 5th and 95th percentiles. In the lower panels, the X-axis shows the observation numbers. The rest of the plot information is the same as described in the upper panel. High and low-depletion years in SH included ozonesondes launched from Ushuaia, Lauder and Macquarie Island.

We observed higher ozone abundances in the NH for the entire period analyzed and for both subperiods, i.e., late winter-early spring and mid-spring compared with the SH **(Fig. 5)**. We also noticed differences between high and low-depletion years in both hemispheres (hereafter referred to as interannual variability). In the NH, ozone interannual variability increased by 9% (31 $\pm$ 11 nmol mol^{-1}) compared with high depletion years. The changes in the subperiods late winter-early spring and mid-spring were similar, with 8% (26 $\pm$ 22 nmol mol^{-1}) and 10% (36 $\pm$ 12 nmol mol^{-1}), respectively.

In the SH, ozone interannual variability was more intense in late winter-early spring, especially for pressures less than 270 hPa. Within 300-200 hPa, the difference between medians averaged 53 ± 17 nmol mol^{-1}, being on average 31% greater relative to high depletion years (**Fig.5**). The observed change in mid-spring was more variable. We attribute this behavior to the shorter time of flight in some pressure bins. On the other hand, 2019 is heavily influenced by the SouthTRAC sample size despite including three ozonesonde sites, as shown in **Figure B1**, where the ozone boxplots are without SouthTRAC data. Interestingly, by excluding SouthTRAC data, the mid-spring period is consistently higher in low depletion years at all pressure bins and reproduced ozone's higher interannual variability in late winter-early spring. Hence, considering only ozonesondes, the enhancement for mid-spring was 17% (33 ± 10 nmol mol^{-1}) and for the entire period (SouthTRAC combined with ozonesondes) it was 24% (43 ± 13 nmol mol^{-1}).

The higher ozone levels observed in the late winter-early spring during the 2002 and 2019 SH SSW (45°-60°S), compared with high depletion years (2002-2022), clearly illustrate the impact of the early warming of the polar vortex in September 2019, which was even earlier than the September 2002 warming (Scambos and Stammerjohn, 2020). In this region, Antarctic ozone depletion, more intense between 12 and 20 km, typically begins in August, accelerates in September, and reaches a minimum in October when ozone starts to recover. Therefore, the period of higher ozone destruction rate in September was entirely captured by the SouthTRAC mission.

Although the magnitude of the SSW event was not categorized as a major event, i.e., easterly winds did not reverse at 10 hPa at 60° S, it was strong enough to decrease the halogen-catalyzed ozone loss over the polar region and be detected in subpolar regions as shown in **Figure 5**. Later, in mid-spring, the observed ozone changes were less intense. Nonetheless, it is worth noting that even during this less ozone-depleted atypical scenario in 2019, the ozone abundance in the UTLS was not comparable to the higher levels observed in the NH, representing only 57% of the NH ozone median.

The agreement between carbon monoxide and 20% RH filters varies with pressure bins, with a better agreement at pressures less than 270 hPa and where more aircraft measurements were available. On average, between 270 and 200 hPa, the percentage difference between both filters was $13 \pm 16\%$ in low depletion years (NH), $15 \pm 8\%$ in high depletion years (NH) and $5 \pm 6\%$ in low depletion years (SH). In the SH, we have compared only the low-depletion years because carbon monoxide was measured only by the SouthTRAC mission. Thereby, **Figure C1** shows the ozone abundances by pressure bins after applying the carbon monoxide filter (<50 nmol mol-1). Similarly to the 20% RH filter, less ozone abundances were observed in the SH during low-depletion years compared with the NH, and a similar pattern can be observed for the ozone interannual variability in the NH.

4.3 Outputs comparison based on in situ measurement and reanalysis

So far, we have provided ozone mixing ratios (in drier air) for the entire longitudinal band without paying attention to spatial asymmetries previously reported in the literature (Škerlak et al., 2014). Therefore, the motivation of this section is to compare

the in situ measurements of ozone, filtered by 20% RH in the UTLS, with the values produced by the CAMS reanalysis over

315 the entire longitudinal band within 45-60° latitude and for low and high depletion years indicated in **Table 2**, aiming to provide a spatially resolved perspective.

Figure 6 shows that the reanalysis reproduces the ozone interhemispheric differences and the interannual variability associated with high and low ozone depletion years. In **Figure 6**, the ozone boxplot is displayed in five pressure bins, determined by the five vertical levels available for CAMS in 300-200 hPa. **Figure 6** also clearly illustrates the similarity between the ozone

320 medians obtained from the CAMS reanalysis and SouthTRAC in the period with the highest number of flights, i.e., late winter-early spring, for pressures below 270 hPa. In contrast, we observed higher fluctuations in the medians corresponding to the mid-spring period. These differences (also discussed in section 4.2) can be explained, in part, due to the lower flight frequency in this period, i.e., six flights during the mid-spring period versus ten in the late winter-early spring period. Regardless, we can observe the similarity of the ozone medians obtained from ozonesondes and the reanalysis for the entire period (less affected

325 by the mid-September SouthTRAC data).
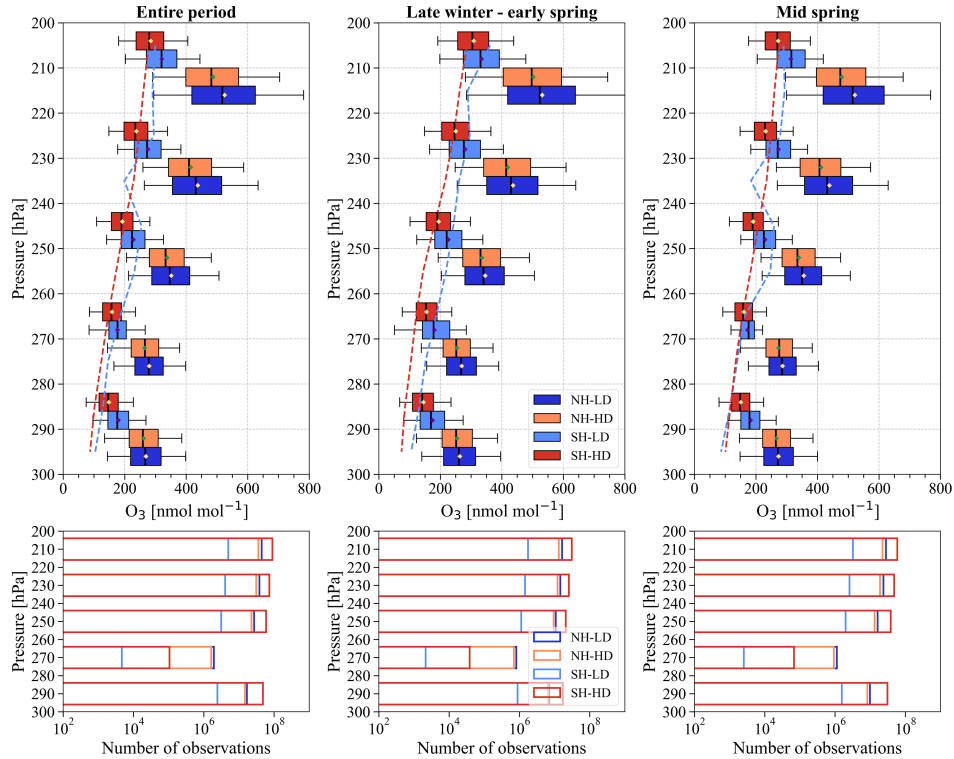
Figure 6: Ozone box plot (nmol mol⁻¹) and associated sample sizes by pressure bins obtained from the CAMS reanalysis. The plots include ozone data with RH less than 20%. The vertical dashed lines are the ozone medians in the SH obtained from ozonesondes and SouthTRAC measurements during high depletion (HD) years (red) and low depletion (LD) years (blue). In the upper panel, the

330 **left, middle and right plots show the entire period, late winter-early spring and mid-spring, respectively, for the northern and southern hemispheres and high-depleted and low-depleted years. Box plots indicate the median, the 25th and 75th percentiles. The diamonds in the upper panels indicate the mean values. The whiskers extend to the 5th and 95th percentiles. In the lower panels, the X-axis shows the observation numbers. The rest of the plot information is the same as described in the upper panel.**

Figure 7 shows CAMS reanalysis across the entire NH and SH longitudinal band for high and low depletion years from 2003 to 2022. Consistently, the spatial distribution of ozone median (filtered by 20% RH) in the UTLS obtained by CAMS reproduced the hemispheric differences discussed previously. In addition, **Figure 7** shows some relevant features related to ozone exchange in the UTLS. In the NH, we observe two regions where the ozone was relatively higher due to lower stratospheric ozone depletion: eastern North America (60°W) and Notheast Asia (140°E). In the SH, under low stratospheric ozone depletion, we observe a large region with relatively higher ozone levels over the southern Indian Ocean and, to a minor degree, the South Pacific Ocean.
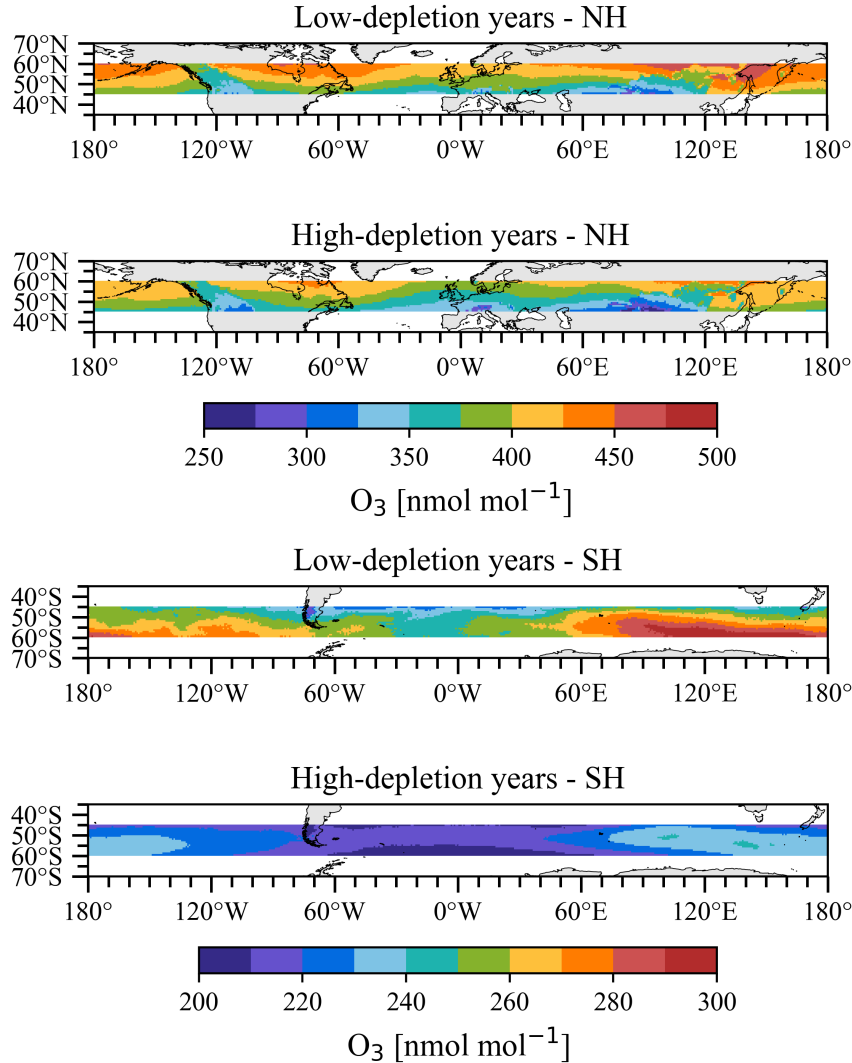
Figure 7: Ozone medians (nmol mol^{-1}) obtained from CAMS reanalysis filtered by RH lower less 20% at a resolution of 0.75° x 0.75° and between 300-200 hPa. The upper panel depicts the ozone median in UTLS of the northern hemisphere, separated into low and high depletion years (entire period), while the lower panel describes the same for the southern hemisphere. Note that the color scales are different in the NH and SH given the strong differences in ozone mixing ratios.

Conclusions

The SouthTRAC mission represents an invaluable contribution to atmospheric chemistry research in the Southern Hemisphere. This aircraft campaign provided unique data recorded during a rare stratospheric sudden warming event in the Southern Hemisphere that produced profound effects on the chemical structure of the atmosphere, leveraged in this research as a proxy for a diminished ozone depletion scenario. The main conclusions of our research are listed below.

Tracer-to-tracer scatterplots between stratospheric ozone and tropospheric tracers (carbon monoxide and water vapor) are consistent with previous airborne campaign studies, which show high ozone and low carbon monoxide levels in the Southern Hemisphere (SH) in both the free troposphere and the upper troposphere-lower stratosphere (UTLS), which in this case was influenced by distant wildfires in Australia.

The bidirectional exchange observed in the UTLS during the 12 Nov 2019 flight provides evidence that transport from tropospheric sources can also influence this region of the atmosphere. During this flight, low levels of nitric acid (<500 pmol mol^{-1}) and hydrogen chloride (<50 pmol mol^{-1}) were consistently measured, alongside higher levels of carbon monoxide (>200 nmol mol^{-1}) and elevated water vapor (>100 µmol mol^{-1}), indicating a strong tropospheric signature in the UTLS.

The comparative analysis of ozone mixing ratios, characterized by stratospheric origin between 300-200 hPa and 45-60° latitude, shows:

i. Lower ozone levels in the SH UTLS compared with the Northern Hemisphere (NH). In high ozone depletion years, defined by the strength of the stratospheric vortex, the ozone median in SH UTLS was 54% of that in the NH UTLS. During years impacted by early stratospheric sudden warming, i.e., low ozone depletion years, the SH UTLS ozone median was 57% of the NH UTLS values.

ii. The interannual ozone variability in the NH UTLS (March-May) as a function of SSW events resulted in a 9% ozone enhancement (31 ± 11 nmol mol^{-1}) compared with years without SSW. This enhancement was nearly three times larger in the SH, reaching 24% (43 ± 13 nmol mol^{-1}).

The chemical reanalysis is especially useful in areas with sparse in situ observations, such as the SH, and its application in this research allows us to assess the representativeness of in-situ observations. Moreover, CAMSRA reproduced the ozone interhemispheric differences and the interannual variability in each hemisphere associated with high and low ozone depletion years. Additionally, the CAMSRA-based analysis identified the southern Indian Ocean as the region with higher ozone in the UTLS.

Finally, differences in spatial coverage between the in situ measurements in the two hemispheres may affect the representativeness of the results and should be considered when interpreting these comparisons. Overall, this study emphasizes the need to expand highly resolved ozone profiles in the upper troposphere and lower stratosphere, particularly across the

375 Southern Hemisphere, where these measurements are crucial for accurately quantifying current stratosphere-troposphere exchange processes and their impact on the tropospheric ozone budget.

Appendix A: Ozone boxplot without RH filter
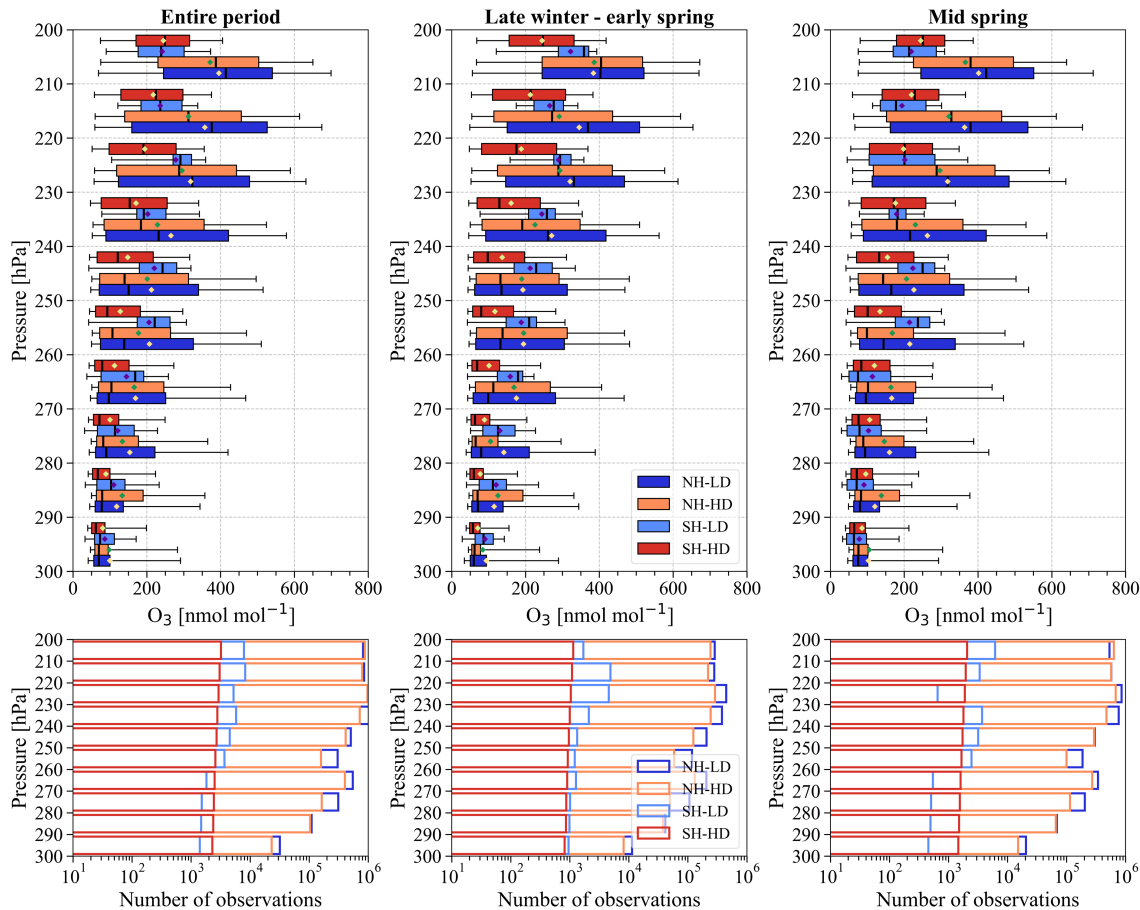
Figure A1: Ozone box plot (nmol mol^{-1}) and associated sample sizes by pressure bins. The plots include ozone data without RH less
380 **than 20% obtained from IAGOS, SouthTRAC and WOUDC (Table 1). In the upper panel, the left, middle and right plots show the entire period, late winter-early spring and mid-spring respectively, for the northern and southern hemispheres and high-depleted (HD) and low-depleted (LD) years. Box plots indicate the median, the 25th and 75th percentiles. The diamonds in the upper panels indicate the mean values. The whiskers extend to the 5th and 95th percentiles. In the lower panels, the X-axis shows the observation numbers. The rest of the plot information is the same as described in the upper panel. High and low-depletion years in SH included**
385 **ozonesondes launched from Ushuaia, Lauder and Macquarie Island.**

390

Appendix B: Ozone boxplot without SouthTRAC data
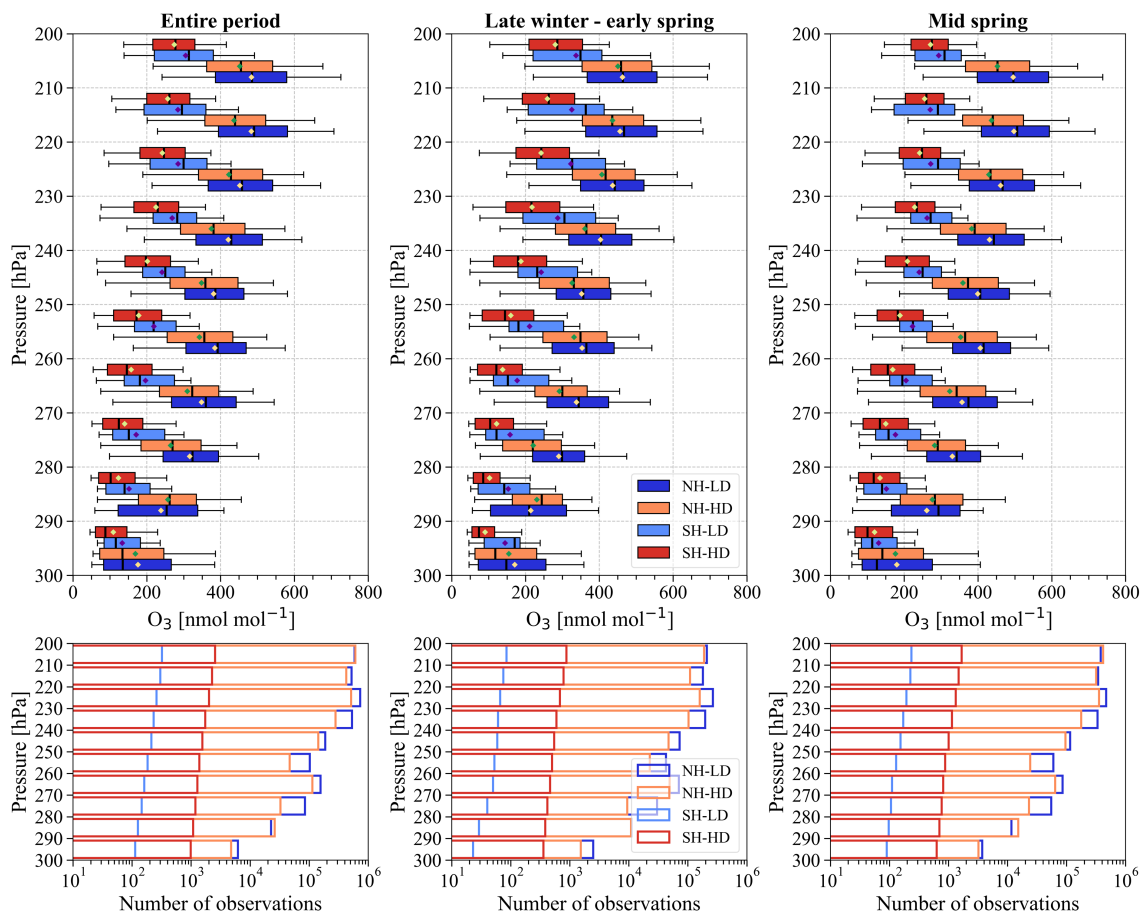
Figure B1: Ozone box plot (nmol mol^{-1}) and associated sample sizes by pressure bins. The plots include ozone data with RH less than 20% obtained exclusively from IAGOS and WOUDC (Table 1). In the upper panel, the left, middle and right plots show the entire period, late winter-early spring and mid-spring respectively, for the northern and southern hemispheres and high-depleted (HD) and low-depleted (LD) years. Box plots indicate the median, the 25th and 75th percentiles. The diamonds in the upper panels indicate the mean values. The whiskers extend to the 5th and 95th percentiles. In the lower panels, the X-axis shows the observation numbers. The rest of the plot information is the same as described in the upper panel. High and low-depletion years in SH included ozonesondes launched from Ushuaia, Lauder and Macquarie Island.

395

400

405

Appendix C: Air masses filtered by carbon monoxide
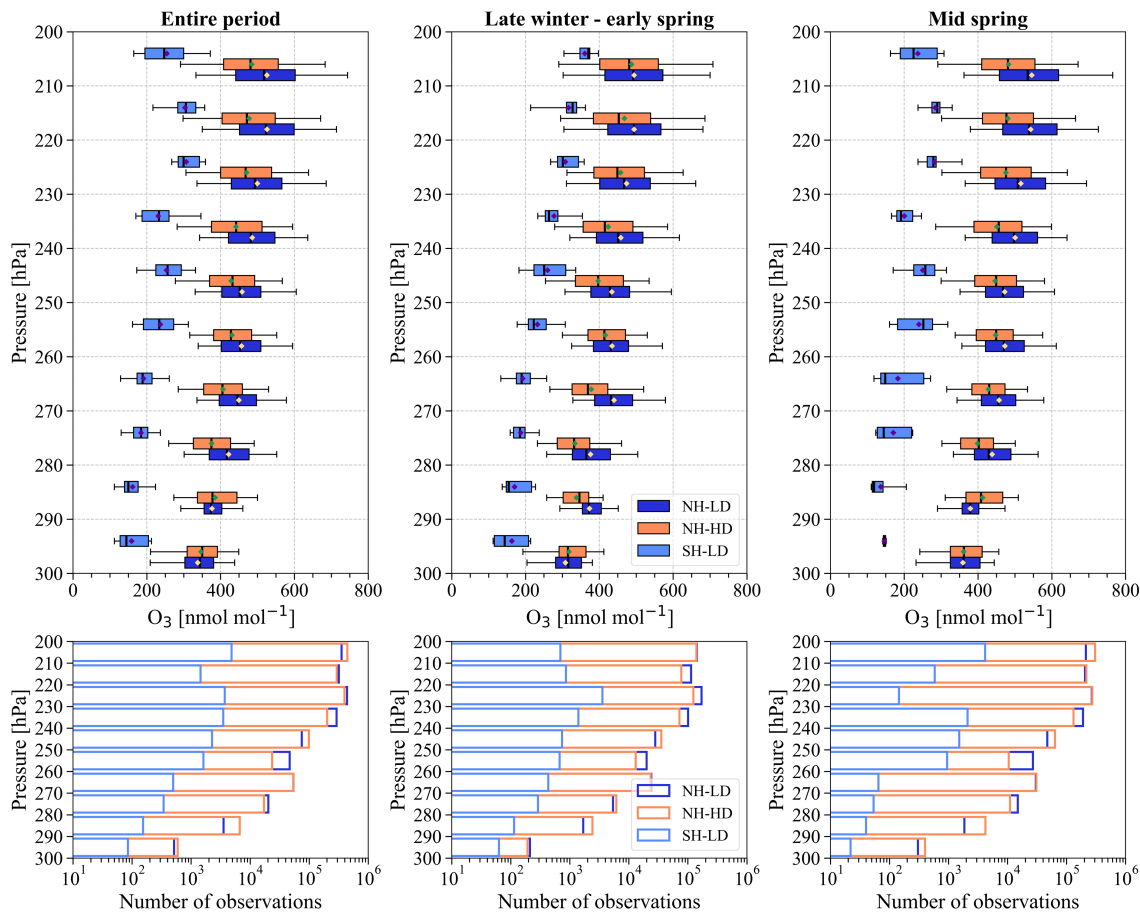
Figure C1: Ozone box plot (nmol mol^{-1}) and associated observation numbers by pressure bins. The plots include ozone data with CO less than 50 nmol mol^{-1}. In the upper panel, the left, middle and right plots show the entire period, late winter-early spring and mid-spring for the northern and southern hemispheres and high-depleted and low-depleted years. Box plots indicate the median, the 25th and 75th percentiles. The diamonds in the upper panels indicate the mean values. The whiskers extend to the 5th and 95th percentiles. In the lower panels, the X-axis shows the observation numbers. The rest of the plot information is the same as described in the upper panel.

425 *Data availability*. SouthTRAC data can be accessed via the HALO database under https://halo-db.pa.op.dlr.de. IAGOS-CARIBIC data can be retrieved at https://zenodo.org/doi/10.5281/zenodo.8188548 (IAGOS-CORE / MOZAIC can be quoted via IAGOS-DB) (Zahn et al., 2024). Ozonesonde data for Ushuaia and Macquarie station can be retrieved from the World Ozone and Ultraviolet Radiation Data Centre (WOUDC) at http://woudc.org/archive/Archive-NewFormat/OzoneSonde_1.0_1/stn339/ecc (WOUDC, 2024). Ozonesonde records for Lauder station were obtained from:

430 Harmonization and Evaluation of Ground Based Instruments for Free Tropospheric Ozone Measurements (HEGIFTOM) at https://hegiftom.meteo.be (HEGIFTOM, 2025). CAMSRA data were obtained from Atmospheric Data Store (ADS): https://ads.atmosphere.copernicus.eu/datasets/cams-global-reanalysis-eac4?tab=overview (ADS, 2025). ERA5 reanalysis were obtained from Copernicus Climate Change Service (C3S) Climate Data Store (CDS) at https://cds.climate.copernicus.eu/datasets/derived-era5-pressure-levels-daily-statistics (C3S/CDS, 2025).

435 *Author contribution*. RS, OC, YC, & CO: conceptualization. OC, CO, YC & RS: methodology. CO & YC: data curation. RS, CO, YC, & OC: formal analysis. RS: writing - original draft preparation. All authors: writing – review & editing. BS & PH initiated and coordinated the SouthTRAC campaign with the HALO research aircraft.

Competing interest. The contact author has declared that none of the authors has any competing interests.

Special issue statement. This article is part of the special issue "Tropospheric Ozone Assessment Report Phase II (TOAR-II)
440 Community Special Issue (ACP/AMT/BG/GMD inter-journal SI)". It is a result of the Tropospheric Ozone Assessment Report, Phase II (TOAR-II, 2020–2024).

Acknowledgments. The authors acknowledge the collaboration provided by the Center for Climate and Resilience Research for the analysis contained in this article (ANID/FONDAP/1523A0002), the supercomputing infrastructure of the NLHPC (ECM-02). The authors thank the pilots, engineers, and scientists from DLR Flight Experiments for their excellent support
445 during the SouthTRAC mission. The authors thank the SouthTRAC member Martin Zoeger (BAHAMAS data). The authors acknowledge that MOZAIC/CARIBIC/IAGOS data were created with support from the European Commission, national agencies in Germany (BMBF), France (MESR), and the UK (NERC), and the IAGOS member institutions (http://www.iagos.org/partners). The participating airlines (Lufthansa, Air France, Austrian, China Airlines, Hawaiian Airlines, Air Canada, Iberia, Eurowings Discover, Cathay Pacific, Air Namibia, Sabena) supported IAGOS by carrying the
450 measurement equipment free of charge since 1994. The data are available at http://www.iagos.fr thanks to additional support from AERIS. The authors thank the following PIs for providing ozonesonde and radiosonde data: Roeland Van Malderen (HEGIFTOM), Richard Querel (Lauder station), Gerardo Carbajal (Ushuaia station) and Matt Tully (Macquarie Island station).

Financial support. This research has been partially supported by ANID (National Agency for Research and Development of Chile, grant no. ANID/FONDAP/1523A0002; ANID-DFG/FONDEQUIP-SouthTRAC/DFG190003;
455 ANID/FONDECYT/1241459. JGU acknowledges funding by the German Science Foundation (Deutsche Forschungsgemeinschaft, DFG) Priority Program SPP 1294: HO4225/15-1, and HO4225/14-1

References

ADS, 2025: https://ads.atmosphere.copernicus.eu/datasets/cams-global-reanalysis-eac4?tab=overview, last access: 11 February 2025.

460 Archibald, A. T., Neu, J. L., Elshorbany, Y. F., Cooper, O. R., Young, P. J., Akiyoshi, H., Cox, R. A., Coyle, M., Derwent, R. G., Deushi, M., Finco, A., Frost, G. J., Galbally, I. E., Gerosa, G., Granier, C., Griffiths, P. T., Hossaini, R., Hu, L., Jöckel, P., Josse, B., Lin, M. Y., Mertens, M., Morgenstern, O., Naja, M., Naik, V., Oltmans, S., Plummer, D. A., Revell, L. E., Saiz-Lopez, A., Saxena, P., Shin, Y. M., Shahid, I., Shallcross, D., Tilmes, S., Trickl, T., Wallington, T. J., Wang, T., Worden, H. M., and Zeng, G.: Tropospheric ozone assessment report: A critical review of changes in the tropospheric

465 ozone burden and budget from 1850 to 2100, https://doi.org/10.1525/elementa.2020.034, 2020.

Atkinson, R.: Atmospheric chemistry of VOCs and NO(x), Atmos Environ, 34, https://doi.org/10.1016/S1352-2310(99)00460-4, 2000.

Bourgeois, I., Peischl, J., Thompson, C. R., Aikin, K. C., Campos, T., Clark, H., Commane, R., Daube, B., Diskin, G. W., Elkins, J. W., Gao, R. S., Gaudel, A., Hintsa, E. J., Johnson, B. J., Kivi, R., McKain, K., Moore, F. L., Parrish, D. D.,

470 Querel, R., Ray, E., Sánchez, R., Sweeney, C., Tarasick, D. W., Thompson, A. M., Thouret, V., Witte, J. C., Wofsy, S. C., and Ryerson, T. B.: Global-scale distribution of ozone in the remote troposphere from the ATom and HIPPO airborne field missions, Atmos Chem Phys, 20, https://doi.org/10.5194/acp-20-10611-2020, 2020.

Brenninkmeijer, C. A. M., Crutzen, P. J., Fischer, H., Güsten, H., Hans, W., Heinrich, G., Heintzenberg, J., Hermann, M., Immelmann, T., Kersting, D., Maiss, M., Nolle, M., Pitscheider, A., Pohlkamp, H., Scharffe, D., Specht, K., and

475 Wiedensohler, A.: CARIBIC-Civil Aircraft for global measurement of trace gases and aerosols in the tropopause region, J Atmos Ocean Technol, 16, https://doi.org/10.1175/1520-0426(1999)016<1373:CCAFGM>2.0.CO;2, 1999.

Brenninkmeijer, C. A. M., Crutzen, P., Boumard, F., Dauer, T., Dix, B., Ebinghaus, R., Filippi, D., Fischer, H., Franke, H., Frieß, U., Heintzenberg, J., Helleis, F., Hermann, M., Kock, H. H., Koeppel, C., Lelieveld, J., Leuenberger, M., Martinsson, B. G., Miemczyk, S., Moret, H. P., Nguyen, H. N., Nyfeler, P., Oram, D., O'Sullivan, D., Penkett, S., Platt, U., Pupek, M.,

480 Ramonet, M., Randa, B., Reichelt, M., Rhee, T. S., Rohwer, J., Rosenfeld, K., Scharffe, D., Schlager, H., Schumann, U., Slemr, F., Sprung, D., Stock, P., Thaler, R., Valentino, F., Van Velthoven, P., Waibel, A., Wandel, A., Waschitschek, K., Wiedensohler, A., Xueref-Remy, I., Zahn, A., Zech, U., and Ziereis, H.: Civil Aircraft for the regular investigation of the atmosphere based on an instrumented container: The new CARIBIC system, Atmos Chem Phys, 7, https://doi.org/10.5194/acp-7-4953-2007, 2007.

485 Butchart, N.: The Brewer-Dobson circulation, https://doi.org/10.1002/2013RG000448, 2014.

C3S/CDS, 2025: https://cds.climate.copernicus.eu/datasets/derived-era5-pressure-levels-daily-statistics, last access 2 February 2025.

Charlton, A. J. and Polvani, L. M.: A new look at stratospheric sudden warmings. Part I: Climatology and modeling benchmarks, J Clim, 20, https://doi.org/10.1175/JCLI3996.1, 2007.

490   Clifton, O. E., Fiore, A. M., Massman, W. J., Baublitz, C. B., Coyle, M., Emberson, L., Fares, S., Farmer, D. K., Gentine, P., Gerosa, G., Guenther, A. B., Helmig, D., Lombardozzi, D. L., Munger, J. W., Patton, E. G., Pusede, S. E., Schwede, D. B., Silva, S. J., Sörgel, M., Steiner, A. L., and Tai, A. P. K.: Dry Deposition of Ozone Over Land: Processes, Measurement, and Modeling, https://doi.org/10.1029/2019RG000670, 2020.

Cooper, O., Forster, C., Parrish, D., Dunlea, E., Hübler, G., Fehsenfeld, F., Holloway, J., Oltmans, S., Johnson, B., Wimmers,

495   A., and Horowitz, L.: On the life cycle of a stratospheric intrusion and its dispersion into polluted warm conveyor belts, Journal of Geophysical Research D: Atmospheres, 109, https://doi.org/10.1029/2003JD004006, 2004.

Dunn, R. J. H., D. M. Stanitski, N. Gobron, and K. M. Willett, Eds., 2020: Global Climate [in "State of the Climate in 2019"]. *Bull. Amer. Meteor.*, 101 (8), S9–S127, https://doi.org/10.1175/BAMS- D-20-0104.1.

Dunn, R. J. H., J. B Miller, K. M. Willett, and N. Gobron, Eds., 2023: Global Climate [in "State of the Climate in 2022"]. Bull.

500   Amer. Meteor. Soc., 104 (9), S11–S145, https://doi.org/10.1175/BAMS-D-23-0090.1.

Dyroff, C., Zahn, A., Christner, E., Forbes, R., Tompkins, A. M., and van Velthoven, P. F. J.: Comparison of ECMWF analysis and forecast humidity data with CARIBIC upper troposphere and lower stratosphere observations, Quarterly Journal of the Royal Meteorological Society, 141, https://doi.org/10.1002/qj.2400, 2015.

Ermel, M., Oswald, R., Mayer, J. C., Moravek, A., Song, G., Beck, M., Meixner, F. X., and Trebs, I.: Preparation methods to

505   optimize the performance of sensor discs for fast chemiluminescence ozone analyzers, Environ Sci Technol, 47, https://doi.org/10.1021/es3040363, 2013.

Forster, P., T. Storelvmo, K. Armour, W. Collins, J.-L. Dufresne, D. Frame, D.J. Lunt, T. Mauritsen, M.D. Palmer, M. Watanabe, M. Wild, and H. Zhang, 2021: The Earth's Energy Budget, Climate Feedbacks, and Climate Sensitivity. In *Climate Change 2021: The Physical Science Basis. Contribution of Working Group I to the Sixth Assessment Report of the*

510   *Intergovernmental Panel on Climate Change* [Masson-Delmotte, V., P. Zhai, A. Pirani, S.L. Connors, C. Péan, S. Berger, N. Caud, Y. Chen, L. Goldfarb, M.I. Gomis, M. Huang, K. Leitzell, E. Lonnoy, J.B.R. Matthews, T.K. Maycock, T. Waterfield, O. Yelekçi, R. Yu, and B. Zhou (eds.)]. Cambridge University Press, Cambridge, United Kingdom and New York, NY, USA, pp. 923–1054, doi:10.1017/9781009157896.009.

Garfinkel, C. I., Aquila, V., Waugh, D. W., and Oman, L. D.: Time-varying changes in the simulated structure of the Brewer-

515   Dobson Circulation, Atmos Chem Phys, 17, https://doi.org/10.5194/acp-17-1313-2017, 2017.

Gettelman, a., Pan, L. L., Randel, W. J., Hoor, P., Birner, T., and Hegglin, M. I.: the Extratropical Upper Troposphere and Lower Stratosphere, Reviews of Geophysics, 49, https://doi.org/10.1029/2011RG000355.1.INTRODUCTION, 2011.

Giez, A., Mallaun, C., Zöger, M., Dörnbrack, A., and Schumann, U.: Static pressure from aircraft trailing-cone measurements and numerical weather-prediction analysis, J Aircr, 54, https://doi.org/10.2514/1.C034084, 2017.

520   Griffiths, P. T., Murray, L. T., Zeng, G., Shin, Y. M., Abraham, N. L., Archibald, A. T., Deushi, M., Emmons, L. K., Galbally, I. E., Hassler, B., Horowitz, L. W., Keeble, J., Liu, J., Moeini, O., Naik, V., O'Connor, F. M., Oshima, N., Tarasick, D., Tilmes, S., Turnock, S. T., Wild, O., Young, P. J., and Zanis, P.: Tropospheric ozone in CMIP6 simulations, Atmos Chem Phys, 21, https://doi.org/10.5194/acp-21-4187-2021, 2021.

Health Effects Institute: State of Global Air 2020. Special Report, MA:Health Effects Instiute, 2020.

525 HEGIFTOM, 2025: https://hegiftom.meteo.be, last access: 11 February 2025.

Helten, M., Smit, H. G. J., Sträter, W., Kley, D., Nedelec, P., Zöger, M., and Busen, R.: Calibration and performance of automatic compact instrumentation for the measurement of relative humidity from passenger aircraft, Journal of Geophysical Research Atmospheres, 103, https://doi.org/10.1029/98JD00536, 1998.

Hersbach, H., Comyn-Platt, E., Bell, B., Berrisford, P., Biavati, G., Horányi, A., Muñoz Sabater, J., Nicolas, J., Peubey, C.,
530 Radu, R., Rozum, I., Schepers, D., Simmons, A., Soci, C., Dee, D., Thépaut, J-N., Cagnazo, C., Cucchi, M. (2023): ERA5 post-processed daily-statistics on pressure levels from 1940 to present. Copernicus Climate Change Service (C3S) Climate Data Store (CDS), DOI: 10.24381/cds.50314f4c

Inness, A., Ades, M., Agustí-Panareda, A., Barr, J., Benedictow, A., Blechschmidt, A. M., Jose Dominguez, J., Engelen, R., Eskes, H., Flemming, J., Huijnen, V., Jones, L., Kipling, Z., Massart, S., Parrington, M., Peuch, V. H., Razinger, M., Remy,
535 S., Schulz, M., and Suttie, M.: The CAMS reanalysis of atmospheric composition, Atmos Chem Phys, 19, https://doi.org/10.5194/acp-19-3515-2019, 2019.

Jensen, M. P., Holdridge, D. J., Survo, P., Lehtinen, R., Baxter, S., Toto, T., and Johnson, K. L.: Comparison of Vaisala radiosondes RS41 and RS92 at the ARM Southern Great Plains site, Atmos. Meas. Tech., 9, 3115–3129, https://doi.org/10.5194/amt-9-3115-2016, 2016

540 Johansson, S., Wetzel, G., Friedl-Vallon, F., Glatthor, N., Höpfner, M., Kleinert, A., Neubert, T., Sinnhuber, B.-M., and Ungermann, J.: Biomass burning pollution in the South Atlantic upper troposphere: GLORIA trace gas observations and evaluation of the CAMS model, Atmos. Chem. Phys., 22, 3675–3691, https://doi.org/10.5194/acp-22-3675-2022, 2022

Jurkat, T., Kaufmann, S., Voigt, C., Schäuble, D., Jeßberger, P., and Ziereis, H.: The airborne mass spectrometer AIMS - Part 2: Measurements of trace gases with stratospheric or tropospheric origin in the UTLS, Atmos Meas Tech, 9,
545 https://doi.org/10.5194/amt-9-1907-2016, 2016.

Kaufmann, S., Voigt, C., Heller, R., Jurkat-Witschas, T., Krämer, M., Rolf, C., Zöger, M., Giez, A., Buchholz, B., Ebert, V., Thornberry, T., and Schumann, U.: Intercomparison of midlatitude tropospheric and lower-stratospheric water vapor measurements and comparison to ECMWF humidity data, Atmos Chem Phys, 18, https://doi.org/10.5194/acp-18-16729-2018, 2018.

550 Kloss, C., Sellitto, P., von Hobe, M., Berthet, G., Smale, D., Krysztofiak, G., Xue, C., Qiu, C., Jégou, F., Ouerghemmi, I., and Legras, B.: Australian Fires 2019–2020: Tropospheric and Stratospheric Pollution Throughout the Whole Fire Season, Front Environ Sci, 9, https://doi.org/10.3389/fenvs.2021.652024, 2021.

Lim, E. P., Hendon, H. H., Butler, A. H., Thompson, D. W. J., Lawrence, Z. D., Scaife, A. A., Shepherd, T. G., Polichtchouk, I., Nakamura, H., Kobayashi, C., Comer, R., Coy, L., Dowdy, A., Garreaud, R. D., Newman, P. A., and Wang, G.: The
555 2019 southern hemisphere stratospheric polar vortex weakening and its impacts, https://doi.org/10.1175/BAMS-D-20-0112.1, 2021.

Lu, X., Zhang, L., Zhao, Y., Jacob, D. J., Hu, Y., Hu, L., Gao, M., Liu, X., Petropavlovskikh, I., McClure-Begley, A., and Querel, R.: Surface and tropospheric ozone trends in the Southern Hemisphere since 1990: possible linkages to poleward expansion of the Hadley circulation, Sci Bull (Beijing), 64, https://doi.org/10.1016/j.scib.2018.12.021, 2019.

Marenco, A., Thouret, V., Nédélec, P., Smit, H., Helten, M., Kley, D., Karcher, F., Simon, P., Law, K., Pyle, J., Poschmann, G., Von Wrede, R., Hume, C., and Cook, T.: Measurement of ozone and water vapor by Airbus in-service aircraft: The MOZAIC airborne program, An overview, https://doi.org/10.1029/98JD00977, 1998.

McConnell, R., Berhane, K., Gilliland, F., London, S. J., Islam, T., Gauderman, W. J., Avol, E., Margolis, H. G., and Peters, J. M.: Asthma in exercising children exposed to ozone: A cohort study, Lancet, 359, https://doi.org/10.1016/S0140-6736(02)07597-9, 2002.

Millán, L. F., Hoor, P., Hegglin, M. I., Manney, G. L., Boenisch, H., Jeffery, P., Kunkel, D., Petropavlovskikh, I., Ye, H., Leblanc, T., and Walker, K.: Exploring ozone variability in the upper troposphere and lower stratosphere using dynamical coordinates, Atmos. Chem. Phys., 24, 7927–7959, https://doi.org/10.5194/acp-24-7927-2024, 2024.

Monks, P. S., Archibald, A. T., Colette, A., Cooper, O., Coyle, M., Derwent, R., Fowler, D., Granier, C., Law, K. S., Mills, G. E., Stevenson, D. S., Tarasova, O., Thouret, V., Von Schneidemesser, E., Sommariva, R., Wild, O., and Williams, M. L.: Tropospheric ozone and its precursors from the urban to the global scale from air quality to short-lived climate forcer, https://doi.org/10.5194/acp-15-8889-2015, 2015.

Müller, S., Hoor, P., Berkes, F., Bozem, H., Klingebiel, M., Reutter, P., Smit, H. G. J., Wendisch, M., Spichtinger, P., and Borrmann, S.: In situ detection of stratosphere-troposphere exchange of cirrus particles in the midlatitudes, Geophys Res Lett, 42, https://doi.org/10.1002/2014GL062556, 2015.

Nédélec, P., Blot, R., Boulanger, D., Athier, G., Cousin, J. M., Gautron, B., Petzold, A., Volz-Thomas, A., and Thouret, V.: Instrumentation on commercial aircraft for monitoring the atmospheric composition on a global scale: The IAGOS system, technical overview of ozone and carbon monoxide measurements, Tellus B Chem Phys Meteorol, 6, https://doi.org/10.3402/tellusb.v67.27791, 2015.

Nedelec, P., Cammas, J. P., Thouret, V., Athier, G., Cousin, J. M., Legrand, C., Abonnel, C., Lecoeur, F., Cayez, G., and Marizy, C.: An improved infrared carbon monoxide analyser for routine measurements aboard commercial Airbus aircraft: Technical validation and first scientific results of the MOZAIC III programme, Atmos Chem Phys, 3, https://doi.org/10.5194/acp-3-1551-2003, 2003.

Neis, P., Smit, H. G. J., Rohs, S., Bundke, U., Krämer, M., Spelten, N., Ebert, V., Buchholz, B., Thomas, K., and Petzold, A.: Quality assessment of MOZAIC and IAGOS capacitive hygrometers: Insights from airborne field studies, Tellus B Chem Phys Meteorol, 6, https://doi.org/10.3402/tellusb.v67.28320, 2015.

Neu, J. L., Hegglin, M. I., Tegtmeier, S., Bourassa, A., Degenstein, D., Froidevaux, L., Fuller, R., Funke, B., Gille, J., Jones, A., Rozanov, A., Toohey, M., Von Clarmann, T., Walker, K. A., and Worden, J. R.: The SPARC data initiative: Comparison of upper troposphere/lower stratosphere ozone climatologies from limb-viewing instruments and the nadir-viewing tropospheric emission spectrometer, J Geophys Res, 119, https://doi.org/10.1002/2013JD020822, 2014.

Ohyama, H., Mizuno, A., Zamorano, F., Sugita, T., Akiyoshi, H., Noguchi, K., Wolfram, E., Salvador, J., and Benitez, G. C.: Characteristics of Atmospheric Wave-Induced Laminae Observed by Ozonesondes at the Southern Tip of South America, Journal of Geophysical Research: Atmospheres, 123, https://doi.org/10.1029/2018JD028707, 2018.

595 Petzold, A., Thouret, V., Gerbig, C., Zahn, A., Brenninkmeijer, C. A. M., Gallagher, M., Hermann, M., Pontaud, M., Ziereis, H., Boulanger, D., Marshall, J., NéDélec, P., Smit, H. G. J., Friess, U., Flaud, J. M., Wahner, A., Cammas, J. P., Volz-Thomas, A., Thomas, K., Rohs, S., Bundke, U., Neis, P., Berkes, F., Houben, N., Berg, M., Tappertzhofen, M., Blomel, T., Pätz, W., Filges, A., Boschetti, F., Verma, S., Baum, S., Athier, G., Cousin, J. M., Sauvage, B., Blot, R., Clark, H., Gaudel, A., Gressent, A., Auby, A., Fontaine, A., Gautron, B., Bennouna, Y., Petetin, H., Karcher, F., Abonnel, C., Dandin, P., Beswick, K., Wang, K. Y., Rauthe-Schöch, A., Baker, A. K., Riede, H., Gromov, S., Zimmermann, P., Thorenz, U.,
600 Scharffe, D., Koeppel, C., Slemr, F., Schuck, T. J., Umezawa, T., Ditas, J., Cheng, Y., Schneider, J., Williams, J., Neumaier, M., Christner, E., Fischbeck, G., Safadi, L., Petrelli, A., Gehrlein, T., Heger, S., Dyroff, C., Weber, S., Assmann, D., Rubach, F., Weigelt, A., Stratmann, G., Stock, P., Penth, L., Walter, D., Heue, K. P., Allouche, Y., Marizy, C., Hermira, J., Bringtown, S., Saueressig, G., Seidel, N., Huf, M., Waibel, A., Franke, H., Klaus, C., Stosius, R., Baumgardner, D., Braathen, G., Paulin, M., and Garnett, N.: Global-scale atmosphere monitoring by in-service aircraft - current achievements
605 and future prospects of the European Research Infrastructure IAGOS, Tellus B Chem Phys Meteorol, 6, https://doi.org/10.3402/tellusb.v67.28452, 2015.

Rao, J., Garfinkel, C. I., White, I. P., and Schwartz, C.: The Southern Hemisphere Minor Sudden Stratospheric Warming in September 2019 and its Predictions in S2S Models, Journal of Geophysical Research: Atmospheres, 125, https://doi.org/10.1029/2020JD032723, 2020.

610 Rapp, M., Kaifler, B., Dörnbrack, A., Gisinger, S., Mixa, T., Reichert, R., Kaifler, N., Knobloch, S., Eckert, R., Wildmann, N., Giez, A., Krasauskas, L., Preusse, P., Geldenhuys, M., Riese, M., Woiwode, W., Friedl-Vallon, F., Sinnhuber, B. M., De la Torre, A., Alexander, P., Hormaechea, J. L., Janches, D., Garhammer, M., Chau, J. L., Federico Conte, J., Hoor, P., and Engel, A.: Southtrac-gw: An airborne field campaign to explore gravity wave dynamics at the world's strongest hotspot, Bull Am Meteorol Soc, 102, https://doi.org/10.1175/BAMS-D-20-0034.1, 2021.

615 Riese, M., Ploeger, F., Rap, A., Vogel, B., Konopka, P., Dameris, M., and Forster, P.: Impact of uncertainties in atmospheric mixing on simulated UTLS composition and related radiative effects, Journal of Geophysical Research Atmospheres, 117, https://doi.org/10.1029/2012JD017751, 2012.

Rolf, C., Afchine, A., Bozem, H., Buchholz, B., Ebert, V., Guggenmoser, T., Hoor, P., Konopka, P., Kretschmer, E., Müller, S., Schlager, H., Spelten, N., Sumiáska-Ebersoldt, O., Ungermann, J., Zahn, A., and Krämer, M.: Transport of Antarctic
620 stratospheric strongly dehydrated air into the troposphere observed during the HALO-ESMVal campaign 2012, Atmos Chem Phys, 15, https://doi.org/10.5194/acp-15-9143-2015, 2015.

Rolf, C., Rohs, S., Smit, H. G. J., Krämer, M., Bozóki, Z., Hofmann, S., Franke, H., Maser, R., Hoor, P., and Petzold, A.: Evaluation of compact hygrometers for continuous airborne measurements, Meteorologische Zeitschrift, 33, https://doi.org/10.1127/metz/2023/1187, 2024.

625 Saunois, M., R. Stavert, A., Poulter, B., Bousquet, P., G. Canadell, J., B. Jackson, R., A. Raymond, P., J. Dlugokencky, E., Houweling, S., K. Patra, P., Ciais, P., K. Arora, V., Bastviken, D., Bergamaschi, P., R. Blake, D., Brailsford, G., Bruhwiler, L., M. Carlson, K., Carrol, M., Castaldi, S., Chandra, N., Crevoisier, C., M. Crill, P., Covey, K., L. Curry, C., Etiope, G., Frankenberg, C., Gedney, N., I. Hegglin, M., Höglund-Isaksson, L., Hugelius, G., Ishizawa, M., Ito, A., Janssens-Maenhout, G., M. Jensen, K., Joos, F., Kleinen, T., B. Krummel, P., L. Langenfelds, R., G. Laruelle, G., Liu, L., MacHida,

630 T., Maksyutov, S., C. McDonald, K., McNorton, J., A. Miller, P., R. Melton, J., Morino, I., Müller, J., Murguia-Flores, F., Naik, V., Niwa, Y., Noce, S., O'Doherty, S., J. Parker, R., Peng, C., Peng, S., P. Peters, G., Prigent, C., Prinn, R., Ramonet, M., Regnier, P., J. Riley, W., A. Rosentreter, J., Segers, A., J. Simpson, I., Shi, H., J. Smith, S., Paul Steele, L., F. Thornton, B., Tian, H., Tohjima, Y., N. Tubiello, F., Tsuruta, A., Viovy, N., Voulgarakis, A., S. Weber, T., Van Weele, M., R. Van Der Werf, G., F. Weiss, R., Worthy, D., Wunch, D., Yin, Y., Yoshida, Y., Zhang, W., Zhang, Z., Zhao, Y., Zheng, B., Zhu,

635 Q., Zhu, Q., and Zhuang, Q.: The global methane budget 2000-2017, Earth Syst Sci Data, 12, https://doi.org/10.5194/essd-12-1561-2020, 2020.

Scambos, T. and Stammerjohn, and S.: State of the Climate in 2019. Antarctica and the Southern Ocean, Bulletin of the American Meteorological Society, 2020.

Scharffe, D., Slemr, F., Brenninkmeijer, C. A. M., and Zahn, A.: Carbon monoxide measurements onboard the CARIBIC
640 passenger aircraft using UV resonance fluorescence, Atmos Meas Tech, 5, https://doi.org/10.5194/amt-5-1753-2012, 2012.

Skeie, R. B., Myhre, G., Hodnebrog, Ø., Cameron-Smith, P. J., Deushi, M., Hegglin, M. I., Horowitz, L. W., Kramer, R. J., Michou, M., Mills, M. J., Olivié, D. J. L., Connor, F. M. O., Paynter, D., Samset, B. H., Sellar, A., Shindell, D., Takemura, T., Tilmes, S., and Wu, T.: Historical total ozone radiative forcing derived from CMIP6 simulations, NPJ Clim Atmos Sci, 3, https://doi.org/10.1038/s41612-020-00131-0, 2020.

645 Škerlak, B., Sprenger, M., and Wernli, H.: A global climatology of stratosphere-troposphere exchange using the ERA-Interim data set from 1979 to 2011, Atmos Chem Phys, 14, https://doi.org/10.5194/acp-14-913-2014, 2014.

Smit, H. G. J., Rohs, S., Neis, P., Boulanger, D., Krämer, M., Wahner, A., and Petzold, A.: Technical note: Reanalysis of upper troposphere humidity data from the MOZAIC programme for the period 1994 to 2009, Atmos Chem Phys, 14, https://doi.org/10.5194/acp-14-13241-2014, 2014.

650 Stohl, A., Bonasoni, P., Cristofanelli, P., Collins, W., Feichter, J., Frank, A., Forster, C., Gerasopoulos, E., Gäggeler, H., James, P., Kentarchos, T., Kromp-Kolb, H., Krüger, B., Land, C., Meloen, J., Papayannis, A., Priller, A., Seibert, P., Sprenger, M., Roelofs, G. J., Scheel, H. E., Schnabel, C., Siegmund, P., Tobler, L., Trickl, T., Wernli, H., Wirth, V., Zanis, P., and Zerefos, C.: Stratosphere-troposphere exchange: A review, and what we have learned from STACCATO, Journal of Geophysical Research Atmospheres, 108, https://doi.org/10.1029/2002jd002490, 2003.

655 Stratmann, G., Ziereis, H., Stock, P., Brenninkmeijer, C. A. M., Zahn, A., Rauthe-Schöch, A., Velthoven, P. V., Schlager, H., and Volz-Thomas, A.: NO and NOy in the upper troposphere: Nine years of CARIBIC measurements onboard a passenger aircraft, Atmos Environ, 133, https://doi.org/10.1016/j.atmosenv.2016.02.035, 2016.

Szopa, S., Naik, V., Adhikary, B., Artaxo, P., Berntsen, T., Collins, W.D., Fuzzi, S., Gallardo, L., Kiendler-Scharr, A., Klimont, Z., Liao, H., Unger, N., and Zanis, P.: Short-Lived Climate Forcers. In Climate Change 2021: The Physical Science Basis. Contribution of Working Group I to the Sixth Assessment Report of the Intergovernmental Panel on Climate Change [Masson-Delmotte, V., P. Zhai, A. Pirani, S.L. Connors, C. Péan, S. Berger, N. Caud, Y. Chen, L. Goldfarb, M.I. Gomis, M. Huang, K. Leitzell, E. Lonnoy, J.B.R. Matthews, T.K. Maycock, T. Waterfield, O. Yelekçi, R. Yu, and B. Zhou (eds.)]. Cambridge University Press, Cambridge, United Kingdom and New York, NY, USA, pp. 817–922, doi:10.1017/9781009157896.008, 2021

Thouret, V., Marenco, A., Logan, J. A., Nédélec, P., and Grouhel, C.: Comparisons of ozone measurements from the MOZAIC airborne program and the ozone sounding network at eight locations, https://doi.org/10.1029/98JD02243, 1998.

Van Malderen, R., Thompson, A.M., Kollonige, D.E., Stauffer, R.M., Smit, H.G.J, Chang, K.-L., et al., Global Ground-based Tropospheric Ozone Measurements: Reference Data and Individual Site Trends (2000-2022) from the TOAR-II/HEGIFTOMProject, submitted to ACP, 2024.

WOUDC, 2024: http://woudc.org/archive/Archive-NewFormat/OzoneSonde_1.0_1/stn339/ecc, last access: 31 July 2024

Zahn, A., Christner, E., Van Velthoven, P. F. J., Rauthe-Schöch, A., and Brenninkmeijer, C. A. M.: Processes controlling water vapor in the upper troposphere/lowermost stratosphere: An analysis of 8years of monthly measurements by the IAGOS-CARIBIC observatory, J Geophys Res, 119, https://doi.org/10.1002/2014JD021687, 2014.

Zahn, A., Obersteiner, F., Gehrlein, T., Neumaier, M., Dyroff, C., Förster, E., Sprung, D., Van Velthoven, P., Xueref-Remy, I., Ziereis, H., Bundke, U., Gerbig, C., Scharffe, D., Slemr, F., Weber, S., Hermann, M., Cheng, Y., & Bönisch, H. (2024). IAGOS-CARIBIC MS files collection (v2024.10.28) (2024.10.28) [Data set]. Zenodo: https://zenodo.org/doi/10.5281/zenodo.8188548, last access: 6 May 2023

Zahn, A., Weppner, J., Widmann, H., Schlote-Holubek, K., Burger, B., Kühner, T., and Franke, H.: A fast and precise chemiluminescence ozone detector for eddy flux and airborne application, Atmos Meas Tech, 5, https://doi.org/10.5194/amt-5-363-2012, 2012.

Zeng, G., Querel, R., Shiona, H., Poyraz, D., Van Malderen, R., Geddes, A., Smale, P., Smale, D., Robinson, J., and Morgenstern, O.: Analysis of a newly homogenised ozonesonde dataset from Lauder, New Zealand, Atmos. Chem. Phys., 24, 6413–6432, https://doi.org/10.5194/acp-24-6413-2024, 2024.

Zheng, X. yan, Orellano, P., Lin, H. liang, Jiang, M., and Guan, W. jie: Short-term exposure to ozone, nitrogen dioxide, and sulphur dioxide and emergency department visits and hospital admissions due to asthma: A systematic review and meta-analysis, Environ Int, 150, https://doi.org/10.1016/j.envint.2021.106435, 2021.